

# The Cluster of Galaxies Surrounding Cygnus A

## II. New Velocities and a Dynamical Model

Michael J. Ledlow<sup>1,3</sup>

*Gemini Observatory, Southern Operations Center, AURA, Casilla 603, La Serena, Chile*

Frazer N. Owen<sup>1</sup>

*National Radio Astronomy Observatory<sup>2</sup>, Socorro, NM 87801*

Neal A. Miller<sup>1,4</sup>

*National Radio Astronomy Observatory<sup>2</sup>, Socorro, NM 87801*

### ABSTRACT

We have spectroscopically identified 77 new members of the Cygnus A cluster, bringing the total to 118 galaxies consistent with cluster membership. We use these data combined with the results from X-rays to deduce a dynamical model for the system. The data are consistent with a cluster-cluster merger viewed at a projection angle of 30-45°, 0.2-0.6 Gyr prior to core passage. We estimate the richness of the combined cluster system at Abell richness class 2 or greater, suggesting the merger of two richness class  $\sim 1$  clusters.

*Subject headings:* galaxies:active — galaxies:clusters:individual(Cygnus A) — galaxies: distances and redshifts — galaxies:individual(Cygnus A)

---

<sup>1</sup>Visiting astronomer, Kitt Peak National Observatory, National Optical Astronomy Observatories, operated by AURA, Inc., under cooperative agreement with the National Science Foundation.

<sup>2</sup>The National Radio Astronomy Observatory is operated by Associated Universities, Inc., under contract with the National Science Foundation.

<sup>3</sup>Deceased 5 June 2004. We shall miss his cheerfulness, unfailing good sense, and scientific industry.

<sup>4</sup>Jansky Fellow of the National Radio Astronomy Observatory, located at Johns Hopkins University, Department of Physics and Astronomy, 3400 N. Charles Street, Baltimore, MD 21218

## 1. Introduction

Cygnus A ( $z = 0.056$ ) is the best studied example and prototype of a powerful FR II radio galaxy and is also one of the brightest nearby X-ray sources. Imaging from *Einstein* showed that Cygnus A resides within  $\approx 10^{14} M_{\odot}$  of hot gas nearly  $1h_{75}^{-1}$  Mpc in extent (Arnaud et al. 1984). Cygnus A itself has a very high X-ray luminosity, which classically, has been associated with a strong cooling-flow with a mass inflow rate possibly as high as  $\sim 250 M_{\odot} \text{ yr}^{-1}$  (Reynolds & Fabian 1996). More recent observations of cooling-core clusters with *XMM* and *Chandra*, however, have motivated both alternative explanations for the observed X-ray excess and imply substantially less cool gas than previously thought for these systems (Bregman 2003; Böhringer et al. 2003). While Cygnus A itself has been studied extensively at all wavelengths, very little has been known of the optical properties of the galaxy cluster or group within which Cygnus A is found on account of its low Galactic latitude ( $5^{\circ}$ ) and attendant confusing star field.

In Paper 1 (Owen et al. 1997) we presented 41 new velocity measurements within a  $22'$  square region surrounding Cygnus A. Prior to that work only 4 concordant redshifts were known (Spinrad & Stauffer 1982). The results indicated that Cygnus A was located, but not centered, in a rich (at least Abell richness class 1), high velocity dispersion cluster. While clearly showing substructure suggestive of a cluster merger, the number of velocities was insufficient to develop a dynamical model for the system.

Using *ASCA*, Markevitch et al. (1999) mapped the gas temperature across the cluster and showed the existence of a hot region between Cygnus A and the secondary X-ray peak to the northwest (in the direction of the dynamical centroid). The temperature structure could be explained by a fairly simple model involving the merger of two similar mass subclusters colliding head-on and developing a shock between them.

In this paper, we analyze new imaging and spectroscopy of the Cygnus A cluster. We compare the results of a detailed substructure analysis to the cluster merger model based on the X-ray gas temperature structure. We discuss the new observations in §2. In §3.1 we look for evidence of bimodality in the spatial and velocity distribution of the cluster. A full 1-D, 2-D, and 3-D substructure analysis is presented in §3.2. In §3.3 we calculate a new estimate for the cluster richness and mass, followed by a Discussion of results and comparison to models in §4. Conclusions are summarized in §5.

## 2. Observations

Spectroscopic observations were queue-scheduled on the WIYN 3.5m telescope for semesters 1997B and 1998A with the Hydra-Bench Spectrograph. We used the 400 line grating covering the spectral range 3880-7060 Å with a dispersion of  $1.55 \text{ \AA pixel}^{-1}$  and the Blue Simmons camera. In 1997B three fiber configurations were observed through clouds for 3x20 minute exposures on the nights of 8 and 30 September and 1 October 1997. In 1998A five fiber configurations were observed in clear conditions on the nights of 29 May and 28-29 June 1998. For each fiber configuration we typically assigned 7-8 fibers to alignment stars and 20-25 sky fibers, leaving 60-70 fibers available for galaxy candidates.

In the first 1997B WIYN queue run we targeted 166 different objects. We used our original KPNO 0.9m 22' field centered on Cygnus A from Owen et al. (1997) (Paper 1) supplemented by images from the Digitized Sky Survey to take advantage of the larger field of view of Hydra (1 degree). While these observations were strongly affected by clouds and mostly unsuccessful, we were able to cull 10 new galaxy velocities and confirmed another 4 of the lower S/N spectra from Paper 1. Approximately 70% of the useful spectra turned out to be stars; the poor resolution of the Digitized Sky Survey made galaxy/star separation very difficult in this crowded field. Even with good quality imaging, there is substantial confusion between blended, faint point-sources and the appearance of an extended object, making this one of the most challenging fields for galaxy selection.

Before the subsequent queue run in 1998A, we obtained new *R*-band images at the KPNO 0.9m telescope on 29-30 April 1998 using the 2048x2048 T2KA CCD at a scale of  $0''.68 \text{ pixel}^{-1}$ . To complement the  $22' \times 22'$  image centered on Cygnus A used in Paper 1, we imaged at two new positions<sup>5</sup> (19:58:14 +40:55:43 and 20:00:06 +41:04:42) providing full spatial coverage over the extent of the X-ray emission. The two new images consisted of 4x10 min dithered exposures with a final image quality of  $1''.4$  -  $1''.7$ . Candidate galaxies were identified using FOCAS and inspected individually by eye. Coupled with the FOCAS results, we used the peak-flux as an additional cut on eliminating stars. Priorities for spectroscopic observation were assigned primarily based on the optical magnitude. We targeted 254 galaxy candidates including many of the measured galaxies from Paper 1 which were of low to medium S/N. Having observed the brighter targets in 1997B (suffering more stellar contamination) and coupled with better weather, the 1998A observations were much more successful in finding new galaxy redshifts. From the 1998A data we measured 88 new velocities and re-confirmed at better signal-to-noise 15 of the more questionable objects from Paper 1.

---

<sup>5</sup>All positions in this paper are epoch J2000

Velocities were measured using the IRAF cross-correlation task FXCOR with the exception of a few emission-line objects. Velocity errors were calculated from the Tonry & Davis R-value (Tonry & Davis 1979) as determined by FXCOR. For emission lines, we took the mean observed velocity over the lines and applied a heliocentric correction. We assume an error of  $30 \text{ km sec}^{-1}$  on emission-line velocities.

We imaged the Cygnus A field again on 19 July 1999 in  $R$ -band at the KPNO 0.9m telescope, this time using the 8K x 8K Mosaic camera giving a full one degree field of view with a scale of  $0''.425 \text{ pixel}^{-1}$ . Details of the data reduction, photometry, and astrometry are given in Miller & Owen (2003). The final image is a sum of  $5 \times 5$  min exposures under excellent conditions. The final image quality was  $0''.85$ . We used this image in all subsequent analysis. We measured aperture magnitudes for all new cluster galaxies using a Gunn-Oke (Gunn & Oke 1975) metric aperture of diameter  $26.2 h_{75}^{-1} \text{ kpc}$ . Magnitudes for individual galaxies were calculated using a range of different procedures for handling of foreground stars, which indicated that the subtraction of such objects in the high stellar density field of Cygnus A was the primary source of error in reported magnitudes. These tests indicated a global error of about 0.2 magnitudes for the Gunn-Oke aperture photometry, compared to an error of 0.05 magnitudes in the photometric solution (Miller & Owen 2003). Absolute magnitudes were calculated assuming a Galactic absorption of  $A_R = 0.81$  (Spinrad & Stauffer 1982) and a K-correction of 0.08 magnitudes, using  $H_0 = 75 \text{ km sec}^{-1} \text{ Mpc}^{-1}$  and  $q_0 = 0.1$ . For non-cluster galaxies (spectroscopically confirmed) and newly identified galaxies we used a fixed aperture of  $5''$  diameter. This smaller aperture was chosen in order to reduce the effects of foreground stars. An identical analysis to that performed for the Gunn-Oke photometry indicated a typical error of 0.1 magnitudes for galaxies brighter than  $m_R = 19$ . All magnitudes included in tables and figures have had foreground stars removed from their apertures.

### 3. Results

#### 3.1. Velocity Distribution and Bimodality

In Table 1 we list all new velocities measured from WIYN. Starting from all 139 velocities (including those from Paper 1), we calculated the biweight estimators of location and scale (Beers et al. 1990). We then trimmed the list according to the first-pass  $3\sigma$  rejection about the central velocity and re-computed the biweight estimators on the edited list. This 2nd iteration produced a list of 118 cluster members within a  $3\sigma$  dispersion of the central biweight velocity  $C_{BI} = 19008^{+151}_{-172} \text{ km sec}^{-1}$  ( $z = 0.0634$ ) and biweight scale  $S_{BI} = 1489^{+123}_{-103} \text{ km sec}^{-1}$ , corrected to the rest frame of the cluster. These values compare quite well to those determined in Owen et al. (1997) ( $C_{BI} = 18873, S_{BI} = 1581 \text{ km sec}^{-1}$ ), while we have

increased the number of confirmed cluster members by more than a factor of 2. Cygnus A ( $cz = 16811 \text{ km sec}^{-1}$ ) is therefore offset  $2197 \text{ km sec}^{-1}$  from the mean cluster velocity. For cluster members, Table 1 includes the right ascension and declination (J2000.0), the heliocentric velocity and error estimate, and Gunn-Oke aperture magnitudes. We re-list velocities for 19 galaxies re-observed from Paper 1 for which we have adopted the new velocity measured with WIYN (higher S/N). In all cases but one, the agreement between velocities was within a few hundred  $\text{km sec}^{-1}$  (typically  $1-2\sigma$ ). We also list velocities for 21 background/foreground galaxies and apparent magnitudes within a  $5''$  aperture.

We plot a velocity histogram for the 118 cluster members in figure 1. While qualitatively similar to that in Paper 1, the bimodality suggested by the previous work initially appears much less significant. There is, however, clearly a heavier tail in the distribution in the vicinity of Cygnus A. We calculate the likelihood of a bimodal distribution using the KMM algorithm (Ashman, Bird, & Zepf 1994), which compares the goodness of fit between unimodal or multimodal Gaussian functions and objectively partitions data into sub-populations accordingly. Interestingly, we find that a single Gaussian model is rejected at a significance of  $>99\%$ . The estimated velocity locations of each group are 16648 (group 1; just  $163 \text{ km sec}^{-1}$  offset from Cygnus A) and  $19428 \text{ km sec}^{-1}$  (group 2). The partitioning assigned 23 members to group 1 and 95 to group 2. While this result is quite significant, there was some trouble in making the subgroup assignments with the estimates of correct allocation rates for each group being 76% and 96%, respectively. These results are for the homoscedastic case assuming a common covariance (velocity dispersion squared) where the estimated velocity dispersion for both groups was  $1126 \text{ km sec}^{-1}$ . The results for the heteroscedastic hypothesis (different velocity dispersions) were quite different, suggesting both different mean velocities ( $18131$  and  $19849 \text{ km sec}^{-1}$ ) and mixing ratios (58 and 60 members) for the groups. While still technically significant at the 99% level (note that the probability distribution is not well determined in this case so the significance is not robust), the estimates for the correct overall allocation rate was 78% (73% and 84% for groups 1,2 respectively). The estimated dispersions were also quite different;  $1651$  and  $755 \text{ km sec}^{-1}$  for groups 1 and 2, respectively.

We also used a variant of the traditional KMM code which fits structures based on positions as well as velocities, although it assumes that the covariance among the three attributes is zero (*i.e.*, there is no correlation between position and velocity; Miller et al. 2003). As is the case for the standard KMM, the significance of the multicomponent fits are not easily derived. However, a Monte Carlo shuffling of the velocities is used to determine the frequency at which a randomized dataset fits as well as the observed one. The results, shown in figure 2, were quite similar to those of the heteroscedastic case given above; two groups with mean velocities of  $17648$  ( $N=61$ ) and  $20126 \text{ km sec}^{-1}$  ( $N=57$ ) and dispersions of  $1134$  and  $600 \text{ km sec}^{-1}$  respectively. Note that the velocity distribution of the higher velocity

group appears much more Gaussian-like than the more dispersed, lower-velocity group which includes Cygnus A. In fact, statistical tests performed on this lower-velocity system indicate that its velocity distribution is non-Gaussian.

In summary, the KMM tests indicate that the Cygnus A cluster is poorly fit by a single system. It may be represented by a pair of systems, with one being consistent with a relaxed cluster having a Gaussian velocity distribution and the other (which includes Cygnus A) more difficult to describe. The velocity dispersions of these two systems imply a virial mass ratio of over 3:1. However, based on numbers of assigned galaxies and the observation that the grouping containing Cygnus A is not well described as a virialized system, these two systems may be of comparable richness and hence mass. A model which fits these characteristics will be developed in the ensuing sections.

We show the velocity-coded spatial distribution in figure 3. Square symbols are the galaxies with velocity less than the cluster mean while triangles represent those at greater velocity. Shading is used to indicate the magnitude of the difference between a galaxy's velocity and the cluster mean, with solid symbols for galaxies within  $\pm 1\sigma$  and open symbols for galaxies with a larger velocity differences. For example, Cygnus A has a velocity  $1.5\sigma$  below the mean, and hence is coded as an open-square. Note the significant grouping around Cygnus A, below and slightly to the left of center, which includes seven satellite galaxies with a small dispersion in velocity. Interestingly, the positions of the galaxies in this lower velocity bin (the open squares in figure 3) show a linear alignment along the principle axis of the cluster.

### 3.2. Substructure Tests

We ran a suite of 1D, 2D, and 3D statistical tests in order to assess and quantify the amount and nature of substructure present in the Cygnus A cluster. These tests are defined and explained in detail in Pinkney et al. (1996, hence referred to as P96). Briefly, the 1D tests are performed solely on the galaxy velocities, the 2D tests on galaxy positions, and the 3D tests on both velocities and positions.

Nearly all of the 1D tests produced a significant result, with the main finding being that the velocity distribution is skewed. Averaging over the 3 skewness tests, the distribution is significantly skewed at better than the 98% level. The DIP-stat (Hartigan & Hartigan 1985) tests for consistency with a unimodal population, and returned a 99% significance to deviations from a single Gaussian distribution, consistent with the KMM results discussed above.

The 2D substructure tests are useful for quantifying clumpiness, asymmetries, and elongations in the spatial distribution of galaxies in the cluster. In figure 4 we show adaptively smoothed contours of the galaxy distribution overlaid onto the X-ray emission from the *ROSAT* PSPC. While similar qualitatively to its counterpart in Paper 1, a much more obvious clump of galaxies is now seen near but not centered (offset=72  $h_{75}^{-1}$  kpc) at the position of Cygnus A. The two peaks in the spatial distribution are located at 19:59:30.6 +40:45:02 and 19:59:03.1 +40:49:36 with a separation of 458 $h_{75}^{-1}$  kpc. Similarly, the galaxy distribution traces well the X-ray gas, although this is partly due to selection effects as our imaging data were centered at locations optimized to span the full extent of the intracluster medium (we did target candidates outside this area based on the POSS). Note that the 2nd peak in the X-ray emission (difficult to see with this stretch and in contrast to Cygnus A), is located near 19:58:50.4 +40:52:14 at a projected separation of  $\sim 700h_{75}^{-1}$  kpc. From the 2D substructure tests, all but the AST test (sensitive to non-central clumping) returned significant results (all  $> 99\%$ ), indicating that the spatial distribution is significantly elongated (Fourier elongation test), asymmetric ( $\beta$ -test), and bimodal (Lee2D).

The 3D substructure tests have the null hypothesis of constant mean velocity and dispersion with position. Consistent with the 1D, 2D, and KMM results, we find evidence for significant substructure (Lee 3D, 99.4%;  $\Delta$ , 99%). The remaining 3D tests were less significant than  $\Delta$  and Lee-3D ( $\alpha$ , 94%;  $\alpha_{var}$ , 89%;  $\epsilon$ , 93%). We show in figure 5 the standard  $\Delta$  bubble plot; the symbol size is proportional to the actual  $\delta$  for each galaxy as calculated by the Dressler-Schechtman test, (Dressler & Schechtman 1988). From comparison to figures 3 and 4, we confirm that the clumping responsible for the positive signal (local velocity and/or dispersion are different from global values) is located exactly on the galaxy clump associated with Cygnus-A.

### 3.3. Mass and Richness

We calculated global mass estimates using a projected mass estimator ( $M_{PME}$ ) and the virial theorem ( $M_{VT}$ ), with values of  $M_{PME} = 4.4 \times 10^{15} M_{\odot}$  and  $M_{VT} = 3.0 \times 10^{15} M_{\odot}$ . The larger  $M_{PME}$  is consistent with the findings of P96 when there is a significant projected separation between two merging clusters at an epoch prior to core crossing. P96 found in general that these estimators over-predict the real cluster masses, which are additionally affected by the presence of merging subclusters.

In figure 6 we plot a histogram of the absolute magnitude distribution of cluster galaxies. The magnitudes ( $M_R$ ) were measured within a Gunn-Oke aperture of diameter 26.2 $h_{75}^{-1}$  kpc, on which system  $M_R^* \approx -22.0$ . From inspection of figure 6, one can see our incompleteness

arises around  $M_R^* \approx -20.5$  due to sensitivity limits and our ability to pick out these fainter galaxies for target selection.

In order to get a better estimate for the richness, we have taken advantage of the sub-arcsecond image quality on our  $R$ -band Mosaic frame to locate galaxies not yet identified spectroscopically. We were fairly conservative in classifying objects as galaxies. Over the entire field, we identified 362 additional galaxies which we list in Table 2. In figure 7 we show the spatial distribution of these newly identified galaxies with adaptively smoothed contours as in figure 4 but on a larger scale covering the full Abell radius mapped by our mosaic image. Note that the primary cluster concentration from figure 4 coincides with the peak offset slightly to the east of center in the full-field plot of figure 7. There is also correspondence with the two lowest surface-density peaks in figure 4 with the other two concentrations in figure 7. We indeed see that the missed galaxy distribution traces the same clustering pattern as the cluster members. There is an additional chain of less-dense concentrations from the southeast to southwest not sampled by our spectroscopy. These results suggest that overall, our spectroscopic sampling is quite good.

We followed the general prescription of Abell (1958) to estimate the cluster richness. The Mosaic frame nearly exactly matches one Abell radius ( $R_A \equiv 1'7/z$ , or  $26.8$  for  $z = 0.0634$ ). Including the galaxies from Table 1, we found 394 galaxies within an Abell radius of Cygnus A (19:59:28.3 +40:44:02). Of these, 133 lie within the range  $m_3$  to  $m_3 + 2$  defined by Abell as the measure of richness. In the original paper, Abell estimated contamination due to foreground and background galaxies using nearby field counts. Lacking a direct analog, we simply estimated field galaxies using  $N = \mathcal{N}10^{0.6m}$  where  $\mathcal{N} = 1.26 \times 10^{-5}$  galaxies steradian $^{-1}$  (see Miller & Owen 2003). The corrected count is then 106, placing the Cygnus A cluster in the middle to high range of richness class (RC) 2 clusters. We note that this estimate for contamination by foreground/background objects is consistent with our spectroscopy results, where 118 of 139 galaxies were shown to be cluster members. An even higher richness is quite possible, given our fairly conservative cut on galaxy identification and the likelihood that additional galaxies are hidden by the numerous Galactic stars. Lastly, if the Cygnus A system is an ongoing merger of two clusters of similar mass and richness, this would imply that they are each rich systems of RC=1.

## 4. Discussion

### 4.1. Optical Results: A Dynamical Model

The picture gleaned from the substructure analysis suggests that Cygnus A is the dominant galaxy in a cluster which is currently merging with another subcluster. The fact that we get a consistent picture from each of the KMM, 1D, 2D, and 3D tests allows us to constrain somewhat the expected merger properties.

Depending on which variant of the KMM partitioning scheme is used we find that the velocity separation of the two subclusters is between 1600 and 2600 km sec<sup>-1</sup> (corrected to the rest-frame of the cluster). We find different mixing ratios for the two cases (homoscedastic or heteroscedastic assumption); with equal velocity dispersions the ratio of galaxy members is of order 4 (Cygnus-A being the poorer group) whereas they are nearly equal when the dispersions are fit independently. The projected separation of the subclusters is  $\sim 700 h_{75}^{-1}$  kpc from the X-rays or  $\sim 460 h_{75}^{-1}$  kpc based on the galaxy surface density peak. We compare the properties of the two subclusters using figures 2- 4. The KMM fits suggest that the Cygnus A subcluster is fairly dispersed in velocity whereas the higher velocity peak is more Gaussian. As seen in projection, spatially the two subclusters appear to be well-mixed, although the immediate clumping centered on Cygnus-A is quite significant with a small velocity-spread, well offset from the global mean. And as previously noted, the KMM group which includes Cygnus A also shows an interesting linear alignment between the two subclusters, possibly coincident with the axis of the merger.

Now, we utilize the N-body results and statistics from the substructure tests in P96 to infer a best model for the merger state of this system. P96 note that the 1D, 2D, and 3D tests each have their own strengths and weaknesses so a collective interpretation of their results can reveal an estimate of the merger geometry. The 1D substructure tests are obviously most sensitive when viewed along the merger axis (in our discussion, this is called a projection angle of 0°), and fail to produce significant results for mergers viewed at projection angles greater than  $\approx 60^\circ$ . The 2D tests require a larger projection angle to separate the components, although the size of this angle required to produce significant substructure tests is dependent on the epoch of the merger. Projection angles smaller than  $\approx 30^\circ$  only produce significant results well before or after core passage. The 3D tests are most sensitive to projection angles  $\lesssim 60^\circ$ , similar to the 1D tests. Thus, producing significant substructure results for all three sets of tests requires an intermediate projection angle of  $\sim 30$ -45°. Furthermore, the simulations indicate that larger mass ratios decrease the significance of many tests, further implying a mass ratio of less than 3:1 for the two subclusters. Specifically, the degree of significance of the 2D and 3D substructure tests we observe is only present

in the simulations at times  $\sim$ 0.2-0.6 Gyr prior to core passage, or else significantly after core passage ( $>2$  Gyr). The high velocity dispersion and 3D tests strongly favor the pre core-passage epoch. The 1D results also support a time quite near to core crossing, but do not discriminate between the pre or post-crossing event. The subcluster morphologies are interesting in this context; the Cygnus A subcluster appears dispersed (figure 2) as if the core of the subcluster were lagging behind its member galaxies in the merger. Also note the compact core around Cygnus A, which is responsible for the significant  $\Delta$ -test results (figure 5). Post core-passage, it would seem unlikely that such a core would remain so distinct. The other subcluster appears more Gaussian in velocity space, is quite well mixed spatially with the Cygnus A subcluster, and lacks a well-defined core. It is not clear which of the subclusters is the *primary* in the merger, although the data do not suggest a large mass ratio so the distinction may be irrelevant.

## 4.2. The Picture from X-rays

More details about the likely merger in this system can be found from properties of the X-ray gas. Markevitch et al. (1999)(MSV99) studied X-ray gas temperature maps from ASCA for several nearby merging galaxy clusters, including Cygnus A. MSV99 mapped the X-ray temperature across the cluster from an annulus including the Cygnus A group (Cygnus A was excised from the data before fitting the temperature) in the direction of the 2nd spatial peak (see figure 4). The results indicate a region between the two clusters with  $T \approx 8 - 9$  keV whereas both subclusters are similar at  $T = 4 - 5$  keV. The hot region is consistent with a shocked region resulting from a head-on collision of similar mass clusters. Under this fairly simple geometry and under the approximation of a 1-dimensional shock, MSV99 estimate a subcluster collision velocity of  $2200^{+700}_{-500}$  km sec $^{-1}$ . This value is close to the expected free-fall velocity that two similar mass,  $T \sim 4 - 5$  keV, clusters would achieve by the time that they reached the observed separation. While this simple 1D shock model ignores the physics of the gas in the interaction, MSV99 confirm that the velocity estimate is accurate to about 20% as compared to when hydrodynamical effects are included in the model. Quite interestingly, this predicted velocity matches extremely well the velocity difference of the two subclusters inferred from the optical data (1600-2600 km sec $^{-1}$ ).

More recently, Smith et al. (2002) studied the ICM surrounding Cygnus A with *Chandra*. While the more diffuse X-ray emission extending to the northwest and the 2nd cluster is partially detected on two of the other chips, the sensitivity is insufficient to characterize its properties. For the southwestern half of the X-ray emission in figure 2, however, Smith et al. confirm the ASCA temperature results and compute both the gas mass and total integrated

cluster mass. Within a 500 kpc radius they derive a gas mass of  $1.1 \times 10^{13} M_{\odot}$  and total mass between  $2.0 - 2.8 \times 10^{14} M_{\odot}$  (depending on the central temperature profile). We estimate a factor of 4-5 higher total mass, based on the projected mass from the optical data. However, it is hard to directly compare the two estimates since Smith et al assumed a lower Hubble constant (*i.e.*,  $H_0 = 50 \text{ km s}^{-1}\text{Mpc}^{-1}$ ), and the *Chandra* measurement includes about 1/3 of the full area of the galaxy distribution and extended X-ray emission. Smith et al. (2002) also show a complex temperature distribution for the cluster consistent with an unsettled dynamical situation in the hot gas.

We looked for counterparts to the X-ray point sources detected in the *Chandra* image of Smith et al. (2002). With the exception of Cygnus A itself, we find no identifications with our extended list of galaxies in Tables 1 and 2, which confirms their conclusion that these sources are most likely stars or background objects (*e.g.*, AGNs).

### 4.3. The Cooling-Core and a Cluster Merger?

One other observation to add to this picture is the presence of the cooling-core, *i.e.*, a core with a cooling time much less than a Hubble time, in Cygnus A. While the interpretation of so-called cooling-flow clusters appears to be undergoing revision (Bregman 2003), some aspects of the more classical picture may survive. Cygnus A is a central-dominant galaxy with a central X-ray peak, a negative or flat temperature gradient and positive metallicity gradient toward the core, and presumably sits at the bottom of the local gravitational potential well (Smith et al. 2002). Thus one would expect significant cooling to occur in its core. However, the X-ray spectrum of the core shows a strong power-law continuum to very high energies as expected for a powerful AGN/Quasar (Young et al. 2002). According to current models, it is expected that the powerful radio source may have a significant influence on the cooling properties of the central gas, with the result that the mass deposition rates inferred by the central X-ray excess alone may be over-estimations by more than an order of magnitude (Fabian 2003; Böhringer et al. 2003; Bregman 2003).

Current observations of cooling flows show that high metal abundances are common and thus require large enrichment times to create them (Böhringer et al. 2003). The implication is that cooling cores probably form very early in clusters, are very persistent phenomenon, and likely survive cluster mergers as well as the energy input over the lifetime of the central AGN's. So most mergers must not destroy cooling cores. Consistent with this hypothesis are the observed high frequency of cluster substructure and the frequency of cooling cores seen in large samples of clusters (*e.g.* Jones & Forman 1999). Disturbances may occur as a result of a merger, but may only take the form of a *sloshing* of the central gas. Churazov

et al. (2003) observed the signs of such an event in the Perseus cluster. These authors also argue that the cold, dense, low-entropy core expected to be found in Perseus (and similarly in Cygnus-A) is probably well protected against the penetration of gas from infalling groups or clusters in a merger event.

In an alternative hypothesis, Burns et al. (2003) suggest that cores of cool gas first form in subclusters which then merge to create rich clusters with cool, central X-ray excesses. In this model, cool cores actually form in hierarchical formation along with the clusters themselves. This model is attractive from the point of view of providing sufficient time to produce the observed central metallicities and is consistent with the presence of substantial substructure in these clusters.

Following the more classical picture of cluster cooling flows, Gómez et al. (2002) studied the consequences of head-on 4:1 and 16:1 mass-ratio mergers on existing cooling-flows. Their results indicated that the key parameters to whether the cooling-flow survives such an event were the gas dynamics in the interaction of secondary and primary cluster gas. Those mergers with higher secondary gas densities were found to be the most disruptive. However, even in the cases of strong disruption of the cooling flow, their simulations indicate that the initial increase in the depth of the gravitational potential at core-crossing is insufficient to disrupt the flow. The demise of the cooling flow in these simulations occurred after a time-delay of 1-2 Gyr following core-crossing. Applied to the Cygnus A cluster, the properties inferred from both optical and X-ray do not suggest a dense cluster core for the higher velocity subcluster. So even for a high mass density in the secondary core (which is not supported by the data), the effects on the cooling flow are expected to be minor. Thus the presence of the cooling core in Cygnus A does not argue strongly either way for a pre or post core-crossing epoch. In any case, one would not expect significant disruption, even with the classical cooling flow model.

#### 4.4. A Connection to the Radio Source and AGN?

The existence of the most powerful radio galaxy in the local universe in the midst of a massive, complex, cluster-cluster merger close to core passage, raises the question of whether there is a connection between the two phenomena. Radio sources are believed to be transients. A soft lower limit to the age of  $\sim 10^{6.8-7}$  can be set from synchrotron spectral aging analysis (Carilli & Barthel 1996; Carilli et al. 1991). A more complete physical argument yields an age of  $\sim 4 \times 10^7$  years (Blandford 1996). Thus the current event we are observing seems to have an age shorter than the merger timescale.

However, the dynamics and the morphology of the optical cluster we report in this paper suggest a complex interaction is underway. The X-ray total intensity and temperature imaging add to the already complicated picture. As can be seen in figure 2, Cygnus A is not at the center of the velocity field of the subcluster to which it is assigned membership. Furthermore, as can be seen in figure 3, Cygnus A is not close to spatial center of its subcluster either. However, from figure 4, one can see that it is at the peak of the galaxy counts as well as the the X-ray peak. One does not see the symmetry one might expect based on what we see in other clusters with dense cores.

Thus while the timescales of the merger event do not clearly match the radio event, the large scale environment around Cygnus A does seem unusually disturbed. This situation allows for a variety of physical phenomena which could disturb the Cygnus A galaxy and produce the radio event. Given the large velocities for the individual galaxies and the dense environment around Cygnus A, a major merger of galaxies seems unlikely (e.g. Gnedin 2003). However, a galaxy in a stable orbit around the Cygnus A might be perturbed by a close passage and fall into the central galaxy. Recently, from adaptive optics imaging, Canalizo et al. (2003) have found a secondary point source located just  $0''.4$  (400 pc in projection) southwest of the radio core. The spectral energy distribution of the object is most consistent with the core of a gas-stripped galaxy, likely merging with the giant elliptical host. In comparison to models, these authors speculate that the core of such a galaxy (100-1000 times less massive than the host) might survive a few pericenter passes or a radial encounter, the time-frame for such events being similar (a few  $\times 10^7$  years) to the estimated age of the radio source.

Also the cluster-cluster merger will produce a time- variable tidal field on galaxies or dense clouds near Cygnus A (Gnedin 2003). This could well disrupt a stable environment near Cygnus A and cause material to fall into the core. Infalling HI gas is seen against the nucleus (Conway & Blanco 1995) and recently near-IR spectroscopy has revealed a giant molecular cloud also falling into the core of Cygnus A. (Bellamy & Tadhunter 2004). Thus indirectly the complex cluster environment could be responsible for the extreme AGN we see in Cygnus A.

#### 4.5. A Coherent Picture

The picture which emerges from both the optical and X-rays is a cluster-cluster merger seen in projection at  $30\text{--}45^\circ$  fairly near to core-crossing, The 2D and 3D substructure tests argue for a pre-crossing time-frame, with the level and type of substructure consistent with epochs between 0.2-0.6 Gyr prior to core passage.

The X-ray results from the literature, as discussed in section 4.3, indicate the presence of a bow-shock located between the two subclusters with a temperature enhancement a factor of two higher than the subcluster ICMs. A shock with these conditions is expected to form by gas moving at supersonic speeds as two  $\approx$  equal mass clusters come together and reach a separation of  $\sim 1$  Mpc. Such a shock forms when the leading edge of the infalling cluster is still several hundreds of kpc from the primary cluster core. As the cores come closer together in time, the shock structure would actually become more difficult to discern because of the steep density profile near the core (an issue of contrast). Additionally, the shock will decelerate as the cores merge because of the increase in the ambient gas density. Hence the X-ray results would also seem to argue for a pre core-crossing epoch.

## 5. Conclusions

Cygnus A resides near but offset from the center of a  $RC \geq 2$  cluster which appears to be merging with another similar richness cluster. The implied mass ratio of the two subclusters is of order 2:1 at most, with the Cygnus-A clump being somewhat more massive.

We have spectroscopically identified 74 new members of the Cygnus A cluster, bringing the total to 118 galaxies consistent with cluster membership based on  $3\sigma$  clipping of the velocity distribution. The cluster has a biweight mean velocity  $C_{BI} = 19008^{+151}_{-172}$  km sec $^{-1}$  and biweight scale  $S_{BI} = 1489^{+123}_{-103}$  km sec $^{-1}$  (corrected to the cluster rest frame).

Results from the optical 1D, 2D, and 3D substructure analysis indicate significant bimodality consistent with the merger of two subclusters. The level of substructure seen and the specific tests which detect it are consistent with a pre core-passage epoch, 200-600 Myr from core-crossing. Such a model is independently supported from the X-ray temperature variations and the presence of shock heated gas between the subclusters. The large velocity dispersion of the KMM substructure associated with Cygnus A, the linear spatial distribution of galaxies along the likely merger axis, and the existence of shocked gas between the two cores suggests that we are viewing this system shortly before core passage.

We thank Dr. Elizabeth Rizza for her help with the 1998 imaging data. This research was supported by the Gemini Observatory, which is operated by the Association of Universities for Research in Astronomy, Inc., on behalf of the international Gemini partnership of Argentina, Australia, Brazil, Canada, Chile, the United Kingdom and the United States of America.

## REFERENCES

Abell, G.O. 1958, ApJS, 3, 211

Arnaud, K.A., Fabian, A.C., Eales, S.A., Jones, C., & Forman, W. 1984, MNRAS, 211, 981

Ashman, K.A., Bird, C.M., & Zepf, S.E. 1994, AJ, 108, 2348

Beers, T.C., Flynn, K., & Gebhardt, K. 1990, AJ, 100, 32

Bellamy, M. J. & Tadhunter, C. N. 2004, MNRAS, 353, 105

Bird, C.M. 1995, ApJ, 445, L81

Blandford, R. D. 1996 *Cygnus A – Study of a Radio Galaxy*, Cambridge University Press, Eds C. L. Carilli & D. E. Harris, p264

Böhringer, H., Matsushita, K., Churazov, E., & Finoguenov, A. 2003, Proceedings of *The Riddle of Cooling Flows in Clusters of Galaxies*, Eds. T.H. Reiprich, J.C. Kempner, & N. Soker

Bregman, J.N. 2003, Proceedings of *The Riddle of Cooling Flows in Galaxies and Clusters of Galaxies*, Eds. T.H. Reiprich, J.C. Kempner, & N. Soker

Burns, J.O., Motl, P.M., Norman, M.L., & Bryan, G.L. 2003, Proceedings of *The Riddle of Cooling Flows in Galaxies and Clusters of Galaxies*, Eds. T.H. Reiprich, J.C. Kempner, & N. Soker

Canalizo, G., Max, C., Whysong, D., Antonucci, R., & Dahm, S.E. 2003, ApJ, 597, 823

Carilli, C.L. & Barthel, P.D. 1996, A&A Rev., 7, 1

Carilli, C.L., Perley, R.A., Dreher, J.W., & Leahy, J.P. 1991, ApJ, 383, 554

Churazov, E., Forman, W., Jones, C., Böhringer, H. 2003, ApJ, 590, 225

Conway, J. E. & Blanco, P. R. 1995, ApJ, 449, L131

Dressler, A. & Shectman, S.A. 1988, AJ, 95, 985

Fabian, A.C. 2003, *RevMexAA*, 17, 303

Gnedin, O. Y. 2003, ApJ, 582, 141

Gómez P.L., Loken, C., Roettiger, K., & Burns, J.O. 2002, ApJ, 569, 122

Gunn, J.E. & Oke, J.B. 1975, *ApJ*, 195, 225

Hartigan, J.A. & Hartigan, P.M. 1985, *Annals of Stat*, 13, 70

Jones, C. & Forman, W. 1999, *ApJ*, 511, 65

Markevitch, M., Sarazin, C.L., & Vikhlinin, A. 1999, *ApJ*, 521, 526

Miller, N.A. & Owen, F.N. 2003, *AJ*, 125, 2427

Miller, N.A., Owen, F.N., & Hill, J.M., 2003, *AJ*, 125, 2393

Owen, F.N., Ledlow, M.J., Morrison, G.E., & Hill, J.M. 1997, *ApJ*, 488, L15 (Paper 1)

Pinkney, J., Roettiger, K., Burns, J.O., & Bird, C.M. 1996, *ApJS*, 104, 1

Reynolds, C.S. & Fabian, A.C. 1996, *MNRAS*, 278, 479

Smith, D.A., Wilson, A.S., Arnaud, K.A., Terashima, Y, & Young, A.J. 2002, *ApJ*, 565, 195

Spinrad, H. & Stauffer, J.R. 1982, *MNRAS*, 200, 153

Tonry, J. & Davis, M. 1979, *AJ*, 84, 1511

Young, A.J., Wilson, A.S., Terashima, Y, Arnaud, K.A., & Smith, D.A. 2002, *ApJ*, 564, 176

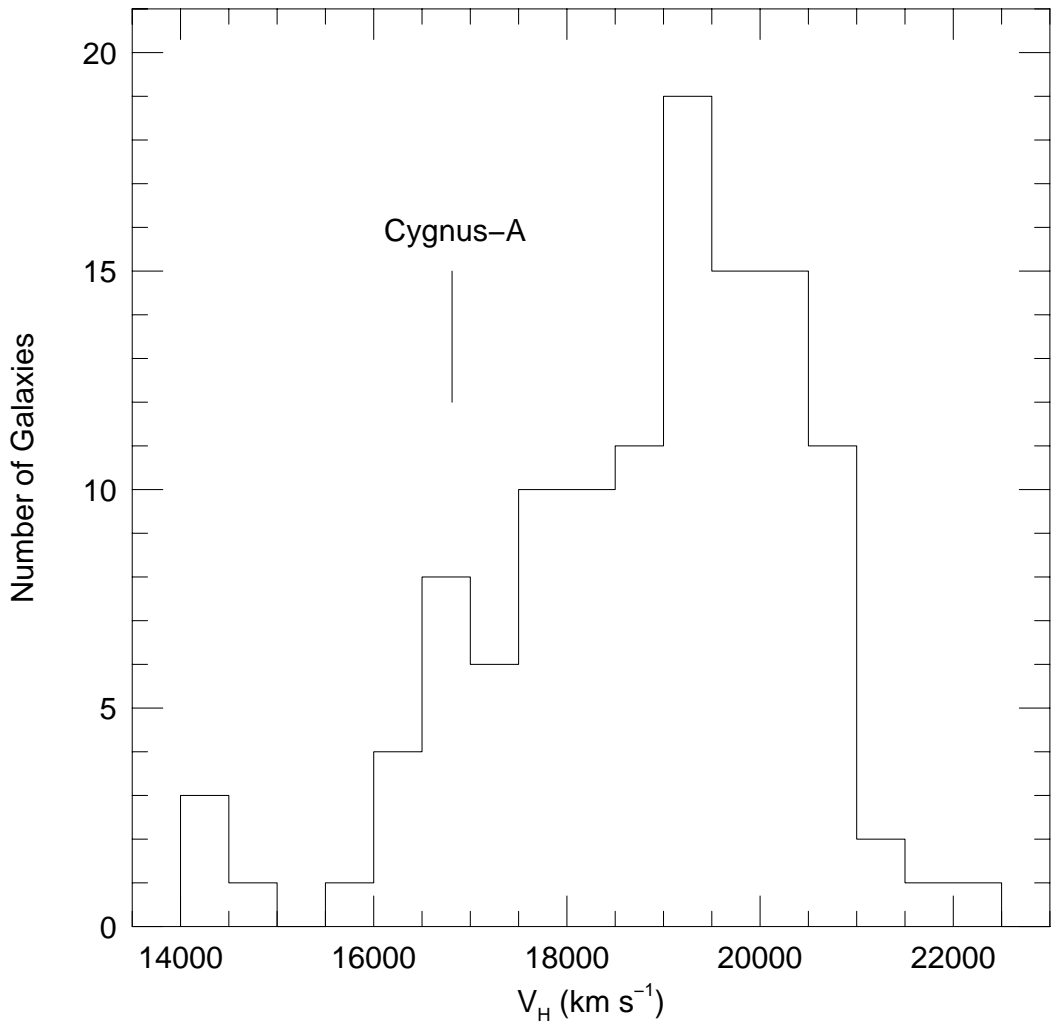


Fig. 1.— Histogram of the radial velocities for all 118 defined cluster members. The binwidth is  $500 \text{ km sec}^{-1}$

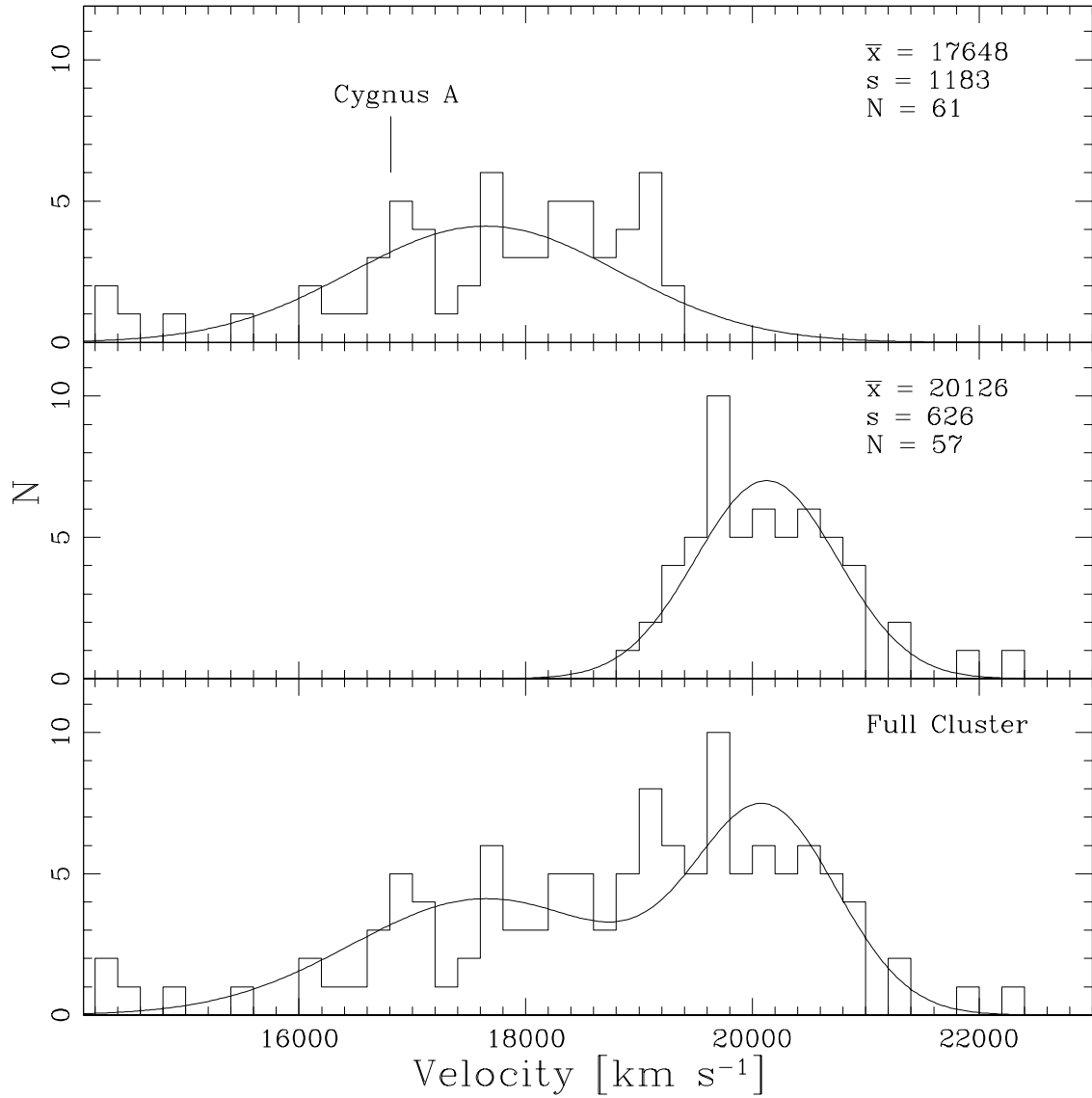


Fig. 2.— Histograms and Gaussians representing the fitted location and dispersions of the two subclusters as separated by the KMM algorithm. The lower panel shows the composite velocity distribution and fits. A velocity binwidth of 200 km sec<sup>-1</sup> was used.

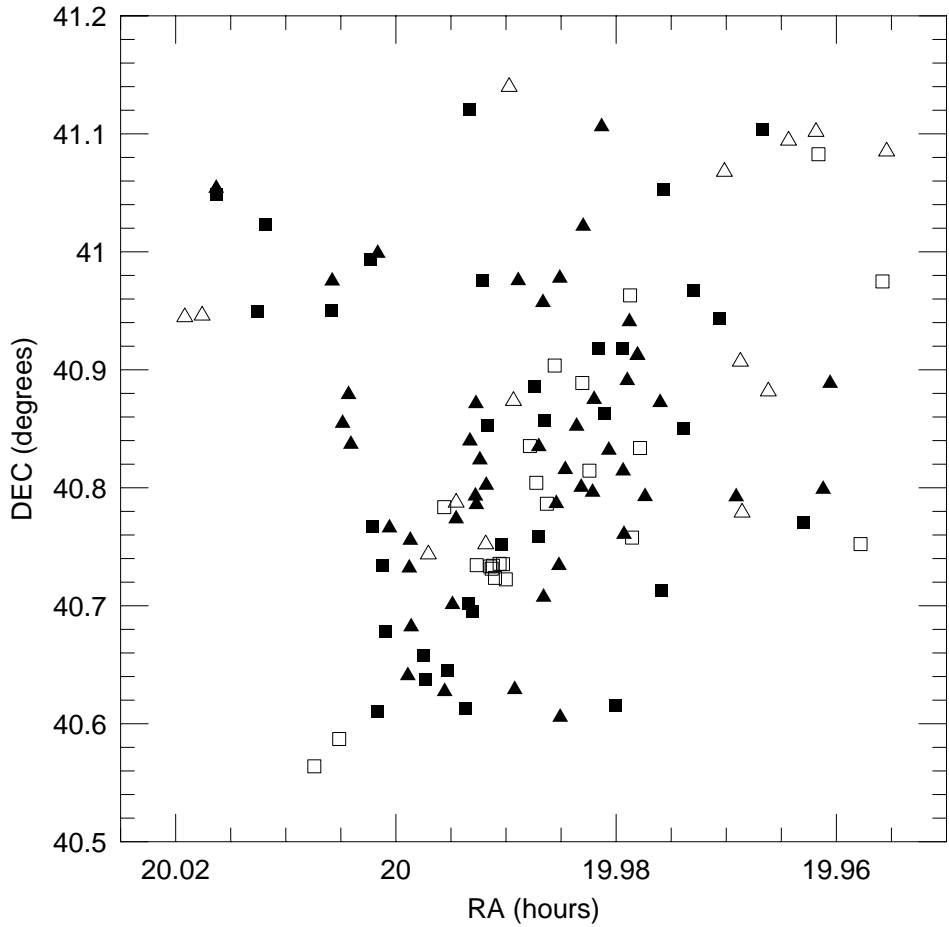


Fig. 3.— Velocity-coded spatial distribution of cluster members. Solid symbols are shown for galaxies with velocities within  $1\sigma$  of the mean (biweight location), open symbols for velocities offset more than  $1\sigma$ . Squares indicate a velocity less than the mean, triangles greater than the mean. The concentration of open-squares below and to the left of center is the Cygnus-A grouping.

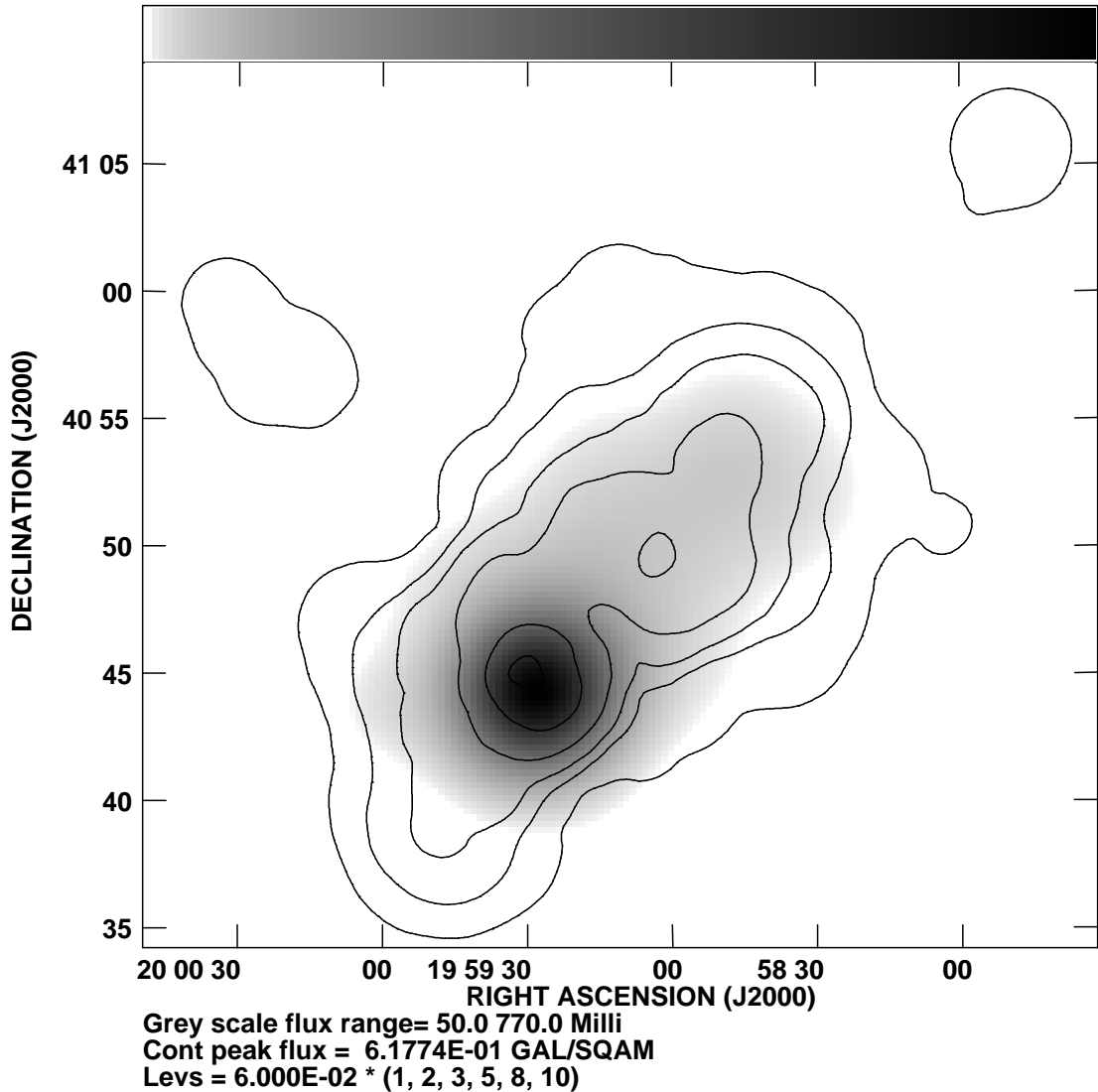


Fig. 4.— Adaptively smoothed galaxy distribution of spectroscopically confirmed cluster members given in Table 1 (contours), superposed on the ROSAT PSPC X-ray image (greyscale). The galaxy density contours are 1,2,3,5,8, and  $10 \times 0.06$  galaxies arcmin<sup>-2</sup>. Cygnus A is located at the X-ray peak of the greyscale image. There is a secondary X-ray peak to the northwest which is difficult to see with this stretch. Its location is noted in the text.

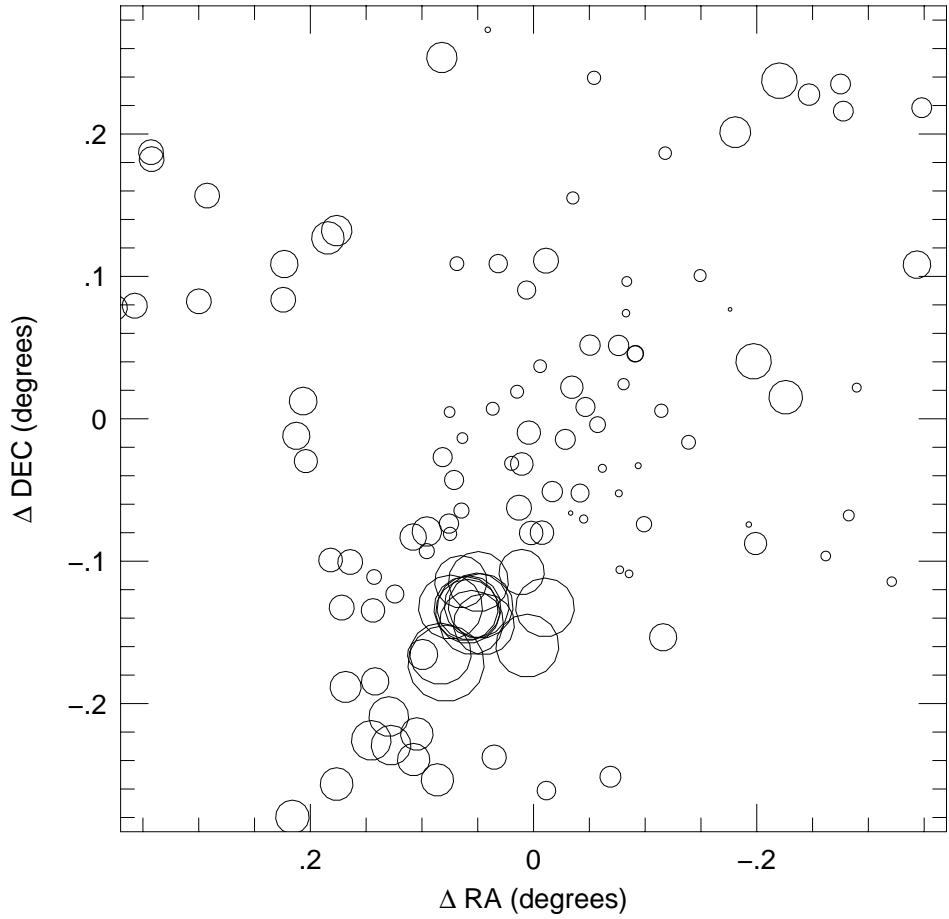


Fig. 5.— Dressler-Shectman bubble-plot showing the results of the  $\Delta$ -test for 3D substructure. The size of the circles are proportional to the  $\delta$ -value calculated for each galaxy. The strong positive signal of subclustering is centered on Cygnus A.

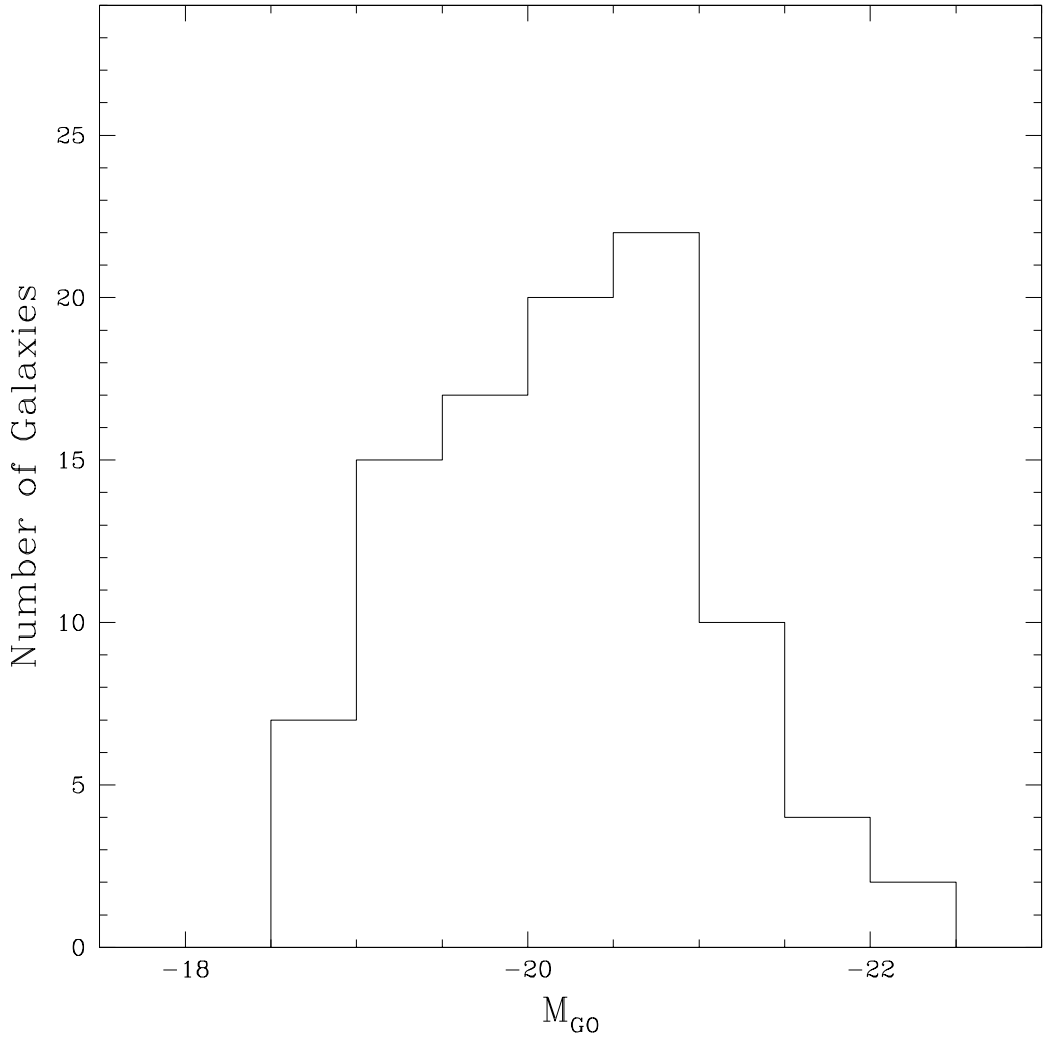


Fig. 6.— Histogram of absolute magnitudes measured within a Gunn-Oke aperture of metric diameter  $26.2h_{75}^{-1}$  kpc for the 118 confirmed cluster members

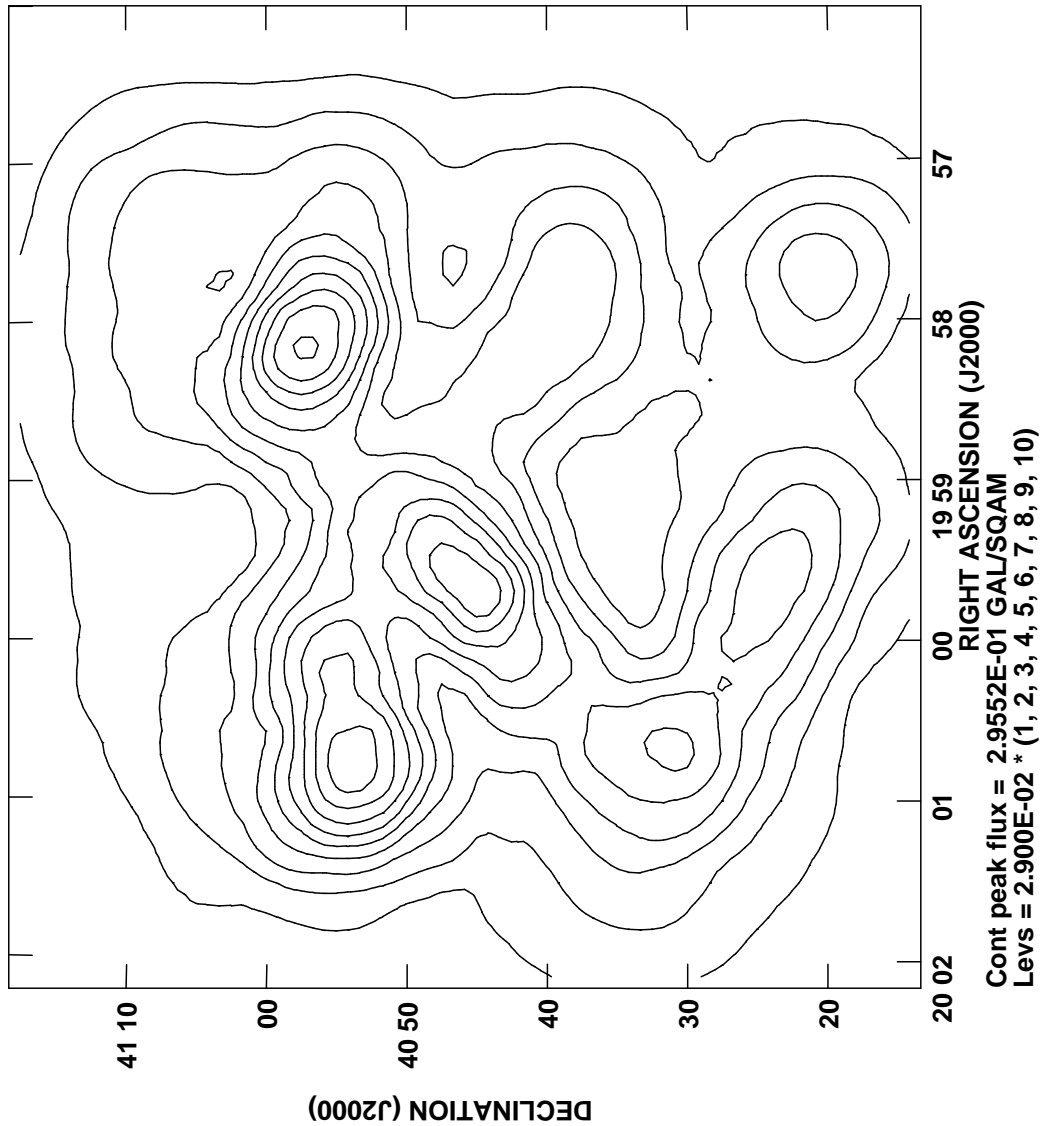


Fig. 7.— Adaptively smoothed contours of the spatial distribution of 362 galaxies identified from the *R*-band Mosaic which were not targeted by spectroscopy. While many of these certainly are background/foreground to the cluster, the surface density in fact matches quite well with our spectroscopic sample (Figure 4), suggesting that our spectroscopic sampling is not strongly biased.

Table 1. Galaxy Velocities and Absolute Magnitudes

RA (J2000)	Dec (J2000)	$v_H$ [km s $^{-1}$ ]	$\Delta v$ [km s $^{-1}$ ]	$M_R$ (GO)
19:57:19.57	41:05:06.5	20986	51	-20.6
19:57:20.93	40:58:29.6	17148	42	-21.4
19:57:28.10	40:45:08.2	14330	88	-19.5
19:57:38.06	40:53:18.8	19786	36	-21.7
19:57:40.32	40:47:55.6	20146	132	-19.2
19:57:41.86	41:04:57.8	14480	112	-19.3
19:57:42.66	41:06:06.3	20806	49	-21.3
19:57:46.87	40:46:13.1	18887	92	-19.6
19:57:51.63	41:05:39.6	20746	59	-20.9
19:57:58.25	40:52:54.4	20596	47	-21.2
19:58:00.04	41:06:14.7	17598	64	-19.3
19:58:06.83	40:46:44.6	20746	30	-20.8
19:58:07.38	40:54:25.2	20746	88	-20.2
19:58:08.75	40:47:32.7	19936	55	-19.8
19:58:12.60	41:04:04.5	22245	80	-18.9
19:58:14.08	40:56:36.6	18797	90	-21.2
19:58:22.60	40:58:02.1	18197	80	-20.8
19:58:25.88	40:51:00.6	17748	47	-20.8
19:58:32.53	41:03:11.6	18257	44	-21.7
19:58:38.55	40:47:33.4	19786	48	-20.4
19:58:40.98	40:54:44.9	19427	65	-20.5
19:58:43.44	40:57:47.1	14330	77	-19.3
19:58:43.67	40:56:27.0	20236	86	-19.5
19:58:44.36	40:53:27.5	20446	60	-20.0
19:58:45.78	40:55:05.4	18557	82	-20.5
19:58:50.38	40:49:54.8	19606	37	-20.5
19:58:51.75	40:51:45.2	17658 <sup>a</sup>	30	-18.6
19:58:52.75	41:06:22.0	20476	72	-20.4
19:58:53.90	40:55:06.2	19007	70	-20.9
19:58:55.20	40:52:29.9	20146	57	-19.6

Table 1—Continued

RA (J2000)	Dec (J2000)	$v_H$ [km s $^{-1}$ ]	$\Delta v$ [km s $^{-1}$ ]	$M_R$ (GO)
19:58:55.70	40:47:46.6	20056	54	-20.8
19:58:58.78	41:01:18.3	19247	62	-20.9
19:58:59.41	40:48:01.7	20476	66	-20.0
19:59:04.63	40:48:55.9	20566	58	-20.1
19:59:06.42	40:58:39.7	19996	92	-19.6
19:59:07.57	40:47:12.1	19307	79	-19.1
19:59:10.64	40:47:11.3	17148	73	-19.0
19:59:11.72	40:42:26.3	19157	79	-19.2
19:59:11.92	40:57:25.4	19457	84	-21.2
19:59:13.34	40:45:32.4	17748	75	-19.8
19:59:14.64	40:53:08.4	18018	96	-20.1
19:59:20.00	40:58:32.3	19157	56	-21.1
19:59:21.16	40:37:44.5	20446	83	-19.1
19:59:21.57	40:52:25.4	21825	111	-18.6
19:59:22.98	41:08:23.5	20626	69	-21.3
19:59:24.07	40:43:20.6	16459	82	-19.9
19:59:24.99	40:44:06.9	16908	62	-20.0
19:59:25.64	40:45:08.3	18377	73	-18.7
19:59:27.60	40:43:25.1	16608	64	-20.4
19:59:28.68	40:43:53.0	16878	78	-20.2
19:59:29.17	40:43:59.9	17388	134	-19.6
19:59:30.18	40:51:11.2	18767	92	-19.5
19:59:30.46	40:48:08.0	19786	72	-19.8
19:59:30.64	40:45:07.9	21345	86	-19.2
19:59:31.76	40:58:32.2	18947	56	-19.6
19:59:33.58	40:44:03.9	16968	159	-19.1
19:59:34.84	40:41:41.8	17928	116	-19.6
19:59:36.04	41:07:13.3	18227	65	-20.8
19:59:40.31	40:46:25.4	20206	61	-19.9
19:59:43.14	40:38:43.0	17778	56	-20.0

Table 1—Continued

RA (J2000)	Dec (J2000)	$v_H$ [km s $^{-1}$ ]	$\Delta v$ [km s $^{-1}$ ]	$M_R$ (GO)
19:59:44.06	40:37:38.4	19277 <sup>a</sup>	30	-18.7
19:59:50.48	40:38:14.8	18107	107	-20.0
19:59:51.12	40:39:27.2	18677	133	-19.5
20:00:04.51	40:44:02.6	19007	90	-20.7
20:00:05.93	40:59:55.6	20056	69	-20.6
20:00:08.44	40:59:37.2	17628	106	-19.4
20:00:15.48	40:52:44.7	19666	156	-19.0
20:00:18.54	40:35:13.5	17418	132	-19.1
20:00:20.83	40:58:31.1	19936	65	-21.0
20:00:21.14	40:57:00.9	18497	69	-20.3
20:00:26.67	40:33:50.2	16638	150	-18.6
20:00:42.78	41:01:24.2	18557	85	-18.9
20:00:45.13	40:56:56.9	17688 <sup>a</sup>	30	-19.9
20:00:58.56	41:02:56.4	18947	96	-20.0
20:00:58.74	41:03:14.0	19487	63	-20.6
20:01:03.35	40:56:45.8	20896	34	-22.1
20:01:09.02	40:56:40.9	20836	68	-21.3
Reobserved Galaxies from Paper 1				
19:58:33.11	40:42:47.5	17898	71	-20.0
19:58:33.63	40:52:20.3	19457	48	-20.6
19:58:40.20	40:50:01.4	16069	45	-20.4
19:58:41.08	40:54:44.0	19337	65	-20.5
19:58:45.43	40:45:38.2	19037	37	-22.3
19:58:45.71	40:48:51.5	20086	49	-21.1
19:58:56.74	40:48:52.2	16159	74	-20.6
19:58:59.07	40:53:19.8	16818	87	-20.4
19:59:00.92	40:51:08.0	19337	52	-21.9
19:59:08.09	40:54:13.0	16668	51	-20.7

Table 1—Continued

RA (J2000)	Dec (J2000)	$v_H$ [km s $^{-1}$ ]	$\Delta v$ [km s $^{-1}$ ]	$M_R$ (GO)
19:59:13.30	40:50:05.7	19367	55	-19.0
19:59:14.10	40:48:15.2	16219	53	-19.3
19:59:16.19	40:50:07.3	15529	54	-20.9
19:59:32.55	40:49:25.3	19636	59	-20.2
19:59:33.83	40:52:17.0	19996	43	-20.2
19:59:55.62	40:43:55.5	20266	98	-20.3
20:00:02.10	40:45:57.8	19067	36	-20.6
20:00:05.96	40:36:36.4	18437	41	-21.9
20:00:07.67	40:46:02.9	17868	115	-19.6
20:00:17.42	40:51:16.9	19187 <sup>b</sup>	50	-20.6
New Non-Cluster Velocities <sup>c</sup>				
19:57:21.93	41:03:38.0	24763	99	18.3
19:57:30.43	40:54:44.1	10373	72	20.4
19:57:38.38	41:01:01.0	41162	105	18.9
19:57:59.78	40:56:59.7	45209	80	20.4
19:57:59.94	40:49:01.0	38764	102	20.0
19:58:08.78	41:06:34.1	31748	90	18.2
19:58:09.35	40:49:36.0	31419	82	19.4
19:58:22.39	41:01:44.2	24613	77	18.8
19:58:22.85	40:58:54.1	5966	77	18.3
19:58:34.89	40:55:32.4	32318	76	18.4
19:58:44.73	40:34:41.7	104540	104	19.8
19:58:46.53	41:05:19.5	41792	70	19.7
19:58:53.89	40:33:19.5	31299	88	19.8
19:58:57.25	40:38:37.3	36006	82	18.8
19:58:57.74	40:59:22.0	26082	82	18.9
19:58:58.35	40:59:39.5	35796	66	19.3
19:59:04.29	40:49:24.8	68294	93	18.2

Table 1—Continued

RA (J2000)	Dec (J2000)	$v_H$ [km s $^{-1}$ ]	$\Delta v$ [km s $^{-1}$ ]	$M_R$ (GO)
19:59:23.50	40:45:45.7	40592	111	19.1
20:00:38.42	40:59:06.7	43830	116	19.9
20:00:41.40	41:00:52.4	13431	94	19.7
20:00:50.58	41:12:14.8	48897	75	20.1

<sup>a</sup>Emission-line redshift.

<sup>b</sup>The velocity for this galaxy was incorrect in Paper 1.

<sup>c</sup>Magnitudes for non-cluster galaxies are apparent magnitudes calculated for a 5" diameter aperture, and are not corrected for Galactic extinction.

Table 2. Missed Galaxies

RA (J2000)	Dec (J2000)	$m_R$ (5'')
19:56:48.41	40:27:52.9	18.1
19:56:48.99	40:56:40.6	18.1
19:56:49.27	40:51:04.6	19.0
19:56:49.28	40:48:48.6	19.4
19:56:51.47	40:34:01.2	19.3
19:56:52.03	40:36:19.0	19.0
19:56:52.57	41:07:43.7	15.8
19:56:53.77	40:27:53.2	19.6
19:56:55.56	40:59:23.2	17.6
19:56:55.82	41:03:51.3	18.4
19:56:58.25	40:20:38.5	19.8
19:57:00.04	40:50:02.7	17.9
19:57:00.74	41:06:17.8	20.3
19:57:00.75	40:48:43.6	18.7
19:57:03.27	40:40:18.2	17.0
19:57:04.00	40:17:04.0	18.7
19:57:04.72	40:14:38.1	19.5
19:57:04.73	41:00:43.2	19.9
19:57:05.45	40:38:30.0	18.5
19:57:05.75	40:15:10.4	17.5
19:57:06.06	41:07:22.3	20.7
19:57:06.12	40:49:53.8	18.3
19:57:06.14	40:57:09.6	17.6
19:57:07.12	40:54:41.8	19.3
19:57:08.16	40:56:11.6	18.8
19:57:08.61	41:11:40.4	18.9
19:57:08.61	41:08:00.8	19.0
19:57:09.11	40:31:13.6	20.0
19:57:09.96	40:52:10.1	16.4
19:57:10.62	41:01:21.6	20.8

Table 2—Continued

RA (J2000)	Dec (J2000)	$m_R$ (5'')
19:57:10.95	40:38:37.0	20.5
19:57:11.72	41:08:15.2	18.5
19:57:12.71	40:38:38.4	20.1
19:57:16.18	40:39:13.5	20.1
19:57:25.40	40:35:19.2	18.8
19:57:26.37	41:02:01.7	20.2
19:57:27.03	41:04:25.5	19.7
19:57:28.11	40:56:26.1	21.2
19:57:28.45	40:55:00.0	20.7
19:57:30.19	40:51:16.4	20.7
19:57:30.72	40:39:00.2	20.3
19:57:32.29	40:14:33.2	19.4
19:57:32.38	40:21:20.0	17.4
19:57:33.30	40:40:48.7	19.9
19:57:33.42	40:30:51.4	20.6
19:57:33.75	41:13:02.7	19.8
19:57:37.40	40:54:05.2	15.3
19:57:37.96	41:09:26.8	18.4
19:57:37.97	40:15:31.6	20.5
19:57:39.52	40:46:39.9	20.2
19:57:39.67	40:36:10.8	20.1
19:57:39.82	41:13:02.1	19.9
19:57:40.61	41:08:46.1	18.8
19:57:41.86	41:10:18.4	18.6
19:57:42.48	40:20:06.9	18.2
19:57:43.72	41:03:27.3	18.7
19:57:43.75	40:19:11.8	16.7
19:57:44.16	41:02:11.5	19.9
19:57:44.93	40:18:09.3	19.8
19:57:45.95	40:21:53.2	20.2

Table 2—Continued

RA (J2000)	Dec (J2000)	$m_R$ (5'')
19:57:46.25	40:34:03.4	18.9
19:57:46.70	40:53:12.1	20.3
19:57:47.94	40:54:38.1	20.7
19:57:48.57	40:41:00.5	19.2
19:57:48.73	41:13:02.9	17.2
19:57:49.52	40:33:39.1	20.9
19:57:49.59	40:22:33.7	17.2
19:57:49.67	40:36:17.3	18.7
19:57:49.94	41:04:54.3	20.1
19:57:50.38	40:25:37.1	18.8
19:57:51.15	40:38:12.2	18.9
19:57:53.82	40:55:10.6	20.9
19:57:53.99	40:14:53.0	19.9
19:57:55.18	40:57:14.5	19.6
19:57:55.70	40:13:39.7	18.9
19:57:57.06	40:42:07.6	20.1
19:57:57.26	41:00:36.1	19.1
19:57:57.59	40:56:17.3	18.0
19:57:59.45	40:57:05.5	18.8
19:58:00.83	40:56:54.9	19.5
19:58:01.10	40:52:51.9	19.0
19:58:01.84	40:38:45.7	17.9
19:58:02.25	40:25:04.6	18.0
19:58:02.25	40:14:48.6	18.4
19:58:03.34	41:06:07.6	20.4
19:58:04.07	40:19:43.1	20.3
19:58:04.97	40:20:11.0	20.3
19:58:04.99	40:55:09.7	17.0
19:58:05.01	40:37:24.4	18.9
19:58:05.59	40:37:01.9	18.7

Table 2—Continued

RA (J2000)	Dec (J2000)	$m_R$ (5'')
19:58:05.70	40:48:52.9	20.6
19:58:06.62	40:55:44.8	19.3
19:58:07.92	40:38:23.9	19.9
19:58:08.38	41:05:14.2	19.6
19:58:08.40	40:54:55.9	18.7
19:58:08.73	40:57:45.4	19.3
19:58:09.38	40:49:35.4	19.4
19:58:09.98	41:12:54.0	19.0
19:58:10.92	40:52:30.4	20.0
19:58:13.98	40:24:38.4	20.7
19:58:14.01	40:54:44.0	19.9
19:58:14.77	40:26:58.6	19.6
19:58:16.27	41:11:59.7	19.9
19:58:16.55	41:00:39.4	20.0
19:58:16.66	40:56:32.9	19.0
19:58:18.88	40:45:22.1	20.3
19:58:19.19	40:43:21.6	18.3
19:58:19.25	40:40:02.9	17.8
19:58:20.32	40:45:22.1	20.8
19:58:20.71	40:57:30.2	20.0
19:58:21.62	40:54:38.7	20.8
19:58:21.96	41:09:49.9	19.0
19:58:22.41	40:57:44.7	19.8
19:58:22.48	41:01:42.6	18.8
19:58:25.57	40:43:30.3	19.8
19:58:26.40	41:02:54.7	20.2
19:58:26.78	41:00:26.4	20.7
19:58:26.84	40:58:47.1	19.9
19:58:27.01	41:13:30.9	18.5
19:58:27.35	40:37:08.0	17.9

Table 2—Continued

RA (J2000)	Dec (J2000)	$m_R$ (5'')
19:58:28.23	40:32:39.7	19.7
19:58:28.85	40:40:04.1	17.7
19:58:29.18	40:34:14.6	19.2
19:58:30.05	41:07:59.0	19.8
19:58:30.64	41:14:13.9	19.5
19:58:32.49	41:05:16.7	17.8
19:58:34.05	40:47:32.6	20.4
19:58:36.32	40:44:58.3	19.7
19:58:38.61	41:10:49.1	20.2
19:58:39.21	40:58:43.1	20.5
19:58:39.47	40:57:08.0	19.2
19:58:39.76	40:57:32.2	18.6
19:58:41.46	40:26:08.0	20.6
19:58:41.61	40:56:56.3	19.4
19:58:42.81	40:22:17.9	18.7
19:58:42.90	40:45:46.1	20.0
19:58:43.76	40:20:08.2	18.7
19:58:43.99	41:06:14.8	21.1
19:58:47.41	40:34:04.4	17.8
19:58:48.43	41:02:25.5	17.6
19:58:48.48	40:16:32.6	18.5
19:58:48.64	40:16:13.2	17.6
19:58:48.66	40:38:53.9	18.7
19:58:49.84	40:25:41.4	20.9
19:58:50.48	40:52:41.7	17.1
19:58:51.28	40:45:48.1	19.7
19:58:51.47	40:27:12.5	17.9
19:58:51.64	40:50:17.8	18.3
19:58:53.22	40:56:16.8	19.5
19:58:53.43	40:59:37.4	19.2

Table 2—Continued

RA (J2000)	Dec (J2000)	$m_R$ (5'')
19:58:53.92	40:33:19.0	19.8
19:58:53.94	40:44:34.1	19.9
19:58:56.09	41:12:50.4	18.7
19:58:56.31	40:51:58.8	19.7
19:58:57.00	40:29:53.1	16.5
19:58:58.08	40:13:42.3	17.7
19:58:58.68	40:41:30.1	20.5
19:58:59.57	41:07:22.3	20.9
19:59:01.38	41:11:18.1	19.6
19:59:03.46	40:56:08.3	20.2
19:59:03.78	40:22:22.2	17.8
19:59:04.23	40:46:56.6	17.8
19:59:04.55	40:51:30.6	19.5
19:59:04.88	40:19:07.1	19.9
19:59:05.26	40:19:18.8	17.1
19:59:05.86	40:54:04.4	20.8
19:59:06.03	40:49:22.8	19.9
19:59:08.69	40:54:35.3	19.7
19:59:11.68	40:52:03.9	20.1
19:59:12.42	40:18:40.2	18.2
19:59:12.46	41:05:01.2	19.7
19:59:13.50	40:16:05.6	20.3
19:59:14.62	40:46:44.9	19.5
19:59:15.21	40:54:43.8	19.1
19:59:15.78	41:08:55.4	19.5
19:59:16.32	41:04:36.3	21.0
19:59:17.51	40:43:58.9	17.8
19:59:17.93	40:22:00.6	20.1
19:59:20.31	40:32:01.1	19.0
19:59:21.68	40:27:01.1	20.4

Table 2—Continued

RA (J2000)	Dec (J2000)	$m_R$ (5'')
19:59:22.09	40:44:23.7	17.2
19:59:22.24	40:25:54.4	19.1
19:59:22.96	40:49:51.0	19.6
19:59:23.89	40:51:43.3	18.9
19:59:24.09	40:50:29.9	19.1
19:59:24.21	40:49:19.9	19.5
19:59:25.64	40:42:44.5	17.5
19:59:26.24	40:44:48.2	19.4
19:59:26.67	40:43:37.1	18.0
19:59:27.15	40:14:40.2	19.7
19:59:28.07	40:44:40.8	18.6
19:59:28.52	40:21:07.1	18.5
19:59:29.01	40:14:13.4	17.9
19:59:31.22	40:24:16.6	17.5
19:59:31.30	40:54:39.7	20.9
19:59:32.07	40:14:30.8	19.4
19:59:33.70	40:24:50.2	20.5
19:59:34.84	40:39:42.8	18.0
19:59:35.33	41:10:40.8	19.5
19:59:35.66	40:45:32.5	17.9
19:59:35.90	40:34:27.1	19.9
19:59:36.66	40:56:42.2	20.6
19:59:37.08	40:51:20.5	19.9
19:59:37.15	40:37:59.3	20.6
19:59:37.91	40:46:03.5	16.9
19:59:38.15	40:47:58.1	19.7
19:59:38.55	40:19:41.5	18.6
19:59:39.85	40:47:21.3	18.1
19:59:43.52	40:46:35.0	17.4
19:59:43.63	40:25:41.2	17.8

Table 2—Continued

RA (J2000)	Dec (J2000)	$m_R$ (5'')
19:59:44.99	41:12:52.4	18.1
19:59:45.00	40:18:22.8	17.7
19:59:45.63	40:40:24.8	17.2
19:59:47.36	40:23:32.2	17.6
19:59:47.44	40:46:37.4	20.2
19:59:48.49	40:58:01.9	17.6
19:59:48.91	40:43:26.7	20.3
19:59:49.07	40:32:18.4	18.6
19:59:49.70	40:55:52.5	19.3
19:59:49.85	40:56:22.4	20.2
19:59:50.47	40:55:14.1	17.5
19:59:51.80	40:53:35.3	19.0
19:59:51.82	41:05:51.9	18.1
19:59:52.28	40:41:36.9	19.8
19:59:52.46	40:49:17.0	18.1
19:59:52.89	40:44:17.7	19.0
19:59:53.90	41:01:25.8	20.5
19:59:54.01	40:24:13.2	18.3
19:59:55.48	40:28:34.6	19.6
19:59:55.56	40:23:17.2	19.1
19:59:56.18	40:48:49.4	20.7
19:59:56.24	40:26:22.9	17.3
19:59:56.45	40:24:55.6	20.1
19:59:56.88	40:30:55.7	18.2
19:59:58.28	40:52:57.6	18.2
19:59:59.77	40:22:04.8	18.7
20:00:00.62	40:46:07.5	18.3
20:00:00.75	40:43:17.0	19.2
20:00:01.28	40:44:57.4	18.2
20:00:02.04	40:39:52.6	19.9

Table 2—Continued

RA (J2000)	Dec (J2000)	$m_R$ (5'')
20:00:02.36	40:57:07.6	20.0
20:00:02.62	40:57:06.1	20.1
20:00:03.24	40:40:46.6	17.2
20:00:03.51	40:24:01.3	19.9
20:00:04.24	40:40:13.5	19.7
20:00:04.25	40:57:27.7	18.7
20:00:04.54	40:41:31.8	20.9
20:00:06.74	41:07:53.6	18.5
20:00:08.54	40:59:52.9	20.2
20:00:10.06	41:08:12.6	20.8
20:00:11.48	40:51:02.2	20.2
20:00:12.60	40:54:18.4	19.3
20:00:12.99	40:17:18.7	19.7
20:00:13.68	40:54:32.1	20.5
20:00:15.08	40:43:32.5	19.8
20:00:15.50	41:10:00.0	19.8
20:00:15.75	40:39:57.0	18.0
20:00:18.03	40:55:34.2	20.8
20:00:18.65	40:24:02.0	19.2
20:00:19.69	40:54:10.1	19.3
20:00:20.24	40:37:12.0	18.7
20:00:20.31	40:51:46.3	17.3
20:00:20.58	40:26:45.1	18.7
20:00:21.94	40:53:57.3	20.8
20:00:23.32	40:31:25.3	19.9
20:00:23.64	40:45:52.1	20.4
20:00:23.69	40:31:21.4	19.6
20:00:23.91	40:32:48.8	19.5
20:00:24.28	41:08:15.0	20.4
20:00:24.37	40:56:26.9	19.7

Table 2—Continued

RA (J2000)	Dec (J2000)	$m_R$ (5'')
20:00:25.24	40:38:26.4	20.6
20:00:27.57	40:40:03.1	20.2
20:00:27.63	41:02:18.7	20.2
20:00:27.82	40:27:55.9	18.7
20:00:28.02	41:02:37.1	19.7
20:00:29.86	40:25:51.4	20.0
20:00:29.99	41:05:54.7	18.8
20:00:30.30	40:46:24.6	17.1
20:00:31.76	40:51:31.6	20.3
20:00:32.87	40:37:46.6	19.9
20:00:33.39	40:52:42.7	18.6
20:00:33.62	40:34:35.6	19.2
20:00:34.51	40:55:49.6	19.8
20:00:34.83	40:34:48.8	17.7
20:00:34.84	40:52:20.7	18.0
20:00:37.51	40:46:45.8	20.1
20:00:39.16	40:50:30.4	18.5
20:00:39.20	41:02:38.4	20.2
20:00:39.51	40:25:43.0	19.6
20:00:40.81	40:57:18.7	18.5
20:00:40.86	40:20:05.3	19.2
20:00:40.92	40:40:48.6	17.6
20:00:43.29	40:18:45.5	19.4
20:00:43.47	40:30:50.6	21.1
20:00:43.81	40:24:46.2	19.4
20:00:45.03	40:51:31.2	20.6
20:00:46.40	40:29:07.7	18.9
20:00:47.43	40:39:55.5	17.6
20:00:47.94	40:33:37.9	19.4
20:00:49.02	40:53:40.3	19.6

Table 2—Continued

RA (J2000)	Dec (J2000)	$m_R$ (5'')
20:00:50.18	40:53:21.1	17.7
20:00:51.39	40:28:38.7	18.0
20:00:51.68	40:46:28.3	18.9
20:00:51.97	40:32:56.1	19.2
20:00:52.07	40:33:28.7	19.2
20:00:52.51	41:01:36.0	19.2
20:00:52.57	40:31:16.5	16.8
20:00:52.67	40:50:32.7	18.0
20:00:53.18	40:54:38.1	20.3
20:00:53.96	40:58:57.2	19.6
20:00:55.08	40:41:14.6	17.9
20:00:55.21	40:44:30.5	18.8
20:00:55.98	40:52:16.3	18.5
20:00:56.02	41:01:54.5	18.5
20:00:56.19	40:32:05.0	21.1
20:00:56.75	40:54:01.7	18.9
20:00:57.56	40:25:33.1	18.3
20:00:59.44	40:23:18.9	19.5
20:01:00.80	40:59:47.8	18.9
20:01:01.44	40:47:55.3	20.1
20:01:01.50	41:10:06.8	16.6
20:01:03.32	41:00:54.0	18.8
20:01:03.95	40:50:49.8	19.9
20:01:04.68	40:40:19.9	18.8
20:01:05.19	40:55:56.0	20.4
20:01:06.35	40:56:35.0	19.7
20:01:06.96	41:09:26.8	19.7
20:01:07.21	40:50:47.8	17.9
20:01:07.21	40:55:01.2	19.5
20:01:07.30	40:50:16.4	18.7

Table 2—Continued

RA (J2000)	Dec (J2000)	$m_R$ (5'')
20:01:08.77	40:35:22.7	19.6
20:01:08.99	40:32:07.0	20.2
20:01:13.39	40:17:05.6	20.2
20:01:14.79	40:33:10.9	19.5
20:01:16.07	40:56:29.7	20.9
20:01:18.09	40:54:48.6	19.9
20:01:18.96	40:52:34.7	20.1
20:01:19.99	40:41:43.0	20.3
20:01:22.90	40:27:21.3	18.5
20:01:23.76	40:26:01.8	17.2
20:01:25.88	41:13:04.0	20.3
20:01:29.64	40:53:22.4	19.1
20:01:30.76	40:29:11.0	19.0
20:01:31.03	40:50:44.8	19.4
20:01:32.02	40:59:55.3	19.2
20:01:33.20	40:37:31.6	18.2
20:01:33.56	41:01:05.3	19.0
20:01:33.57	40:45:14.4	17.6
20:01:35.82	40:59:04.0	19.4
20:01:38.28	40:31:55.1	18.8
20:01:42.30	41:09:25.8	18.1
20:01:42.69	40:38:42.1	19.9
20:01:46.20	40:26:01.3	18.4
20:01:46.75	40:36:00.3	19.5
20:01:47.48	40:30:38.8	20.0
20:01:47.74	41:11:08.2	20.1
20:01:48.00	41:11:05.1	18.3
20:01:48.31	40:35:57.6	20.2
20:01:50.22	40:35:26.7	19.8
20:01:51.72	40:25:22.5	17.4

Table 2—Continued

RA (J2000)	Dec (J2000)	$m_R$ (5'')
20:01:51.83	40:40:04.0	18.6
20:02:04.97	41:07:32.6	18.5